

# Iterative inversion of synthetic travel times successful at recovering sub-surface profiles of supergranular flows

Jishnu Bhattacharya<sup>1</sup>, Shravan M. Hanasoge<sup>1</sup>, Aaron C. Birch<sup>2</sup>, Laurent Gizon<sup>2,3,4</sup>

<sup>1</sup> Tata Institute of Fundamental Research, Mumbai, India

<sup>2</sup> Max Planck Institute for Solar System Research, Justus-von-Liebig-Weg 3, 37077 Göttingen, Germany

<sup>3</sup> Institut für Astrophysik, Georg-August-Universität Göttingen, 37077 Göttingen, Germany

<sup>4</sup> Center for Space Science, NYUAD Institute, New York University Abu Dhabi, Abu Dhabi, UAE

## Abstract

**Aims.** We develop a helioseismic inversion algorithm that can be used to recover sub-surface vertical profiles of 2-dimensional supergranular flows from surface measurements of synthetic wave travel times.

**Methods.** We carry out seismic wave-propagation simulations through a 2-dimensional section of a flow profile that resembles an averaged supergranule, and a starting model that has flows only at the surface. We assume that the wave measurements are entirely without realization noise for the purpose of our test. We expand the vertical profile of the supergranule stream function on a basis of B-splines. We iteratively update the B-spline coefficients of the supergranule model to reduce the travel-times differences observed between the two simulations. We carry out the exercise for four different vertical profiles peaking at different depths below the solar surface.

**Results.** We are able to accurately recover depth profiles of four supergranule models at depths up to 8 – 10 Mm below the solar surface using  $f - p_4$  modes, under the assumption that there is no realization noise. We are able to obtain the peak depth and the depth of the return flow for each model.

**Conclusions.** A basis-resolved inversion performs significantly better than one where the flow field is inverted for at each point in the radial grid. This is an encouraging result and might act as a guide in developing more realistic inversion strategies that can be applied to supergranular flows in the Sun.

**Key words.** Sun: helioseismology – Sun: oscillations – Convection – Methods: numerical

## 1. Introduction

Convective flows on the solar surface exhibit several length scales (Nordlund et al., 2009). Small-scale granules ( $\sim 1$  Mm) are well studied and characterized. The sub-surface profile and physics behind relatively larger scale flows have eluded a convincing explanation. Supergranules — believed to be overturning flows spanning 35 Mm horizontally on average (Hathaway et al., 2000; Rieutord et al., 2008) — remain one of the fronts where sub-surface imaging has had limited success. Sketching a complete picture of a supergranule involves understanding the nature and magnitude of upflows near the cell center, downflows at the edges of the cell, horizontally diverging flows from the center of the cell towards the edge, as well as deeper return flows that might be present. There are several techniques used to study sub-surface flows (see Gizon et al., 2010, and references therein), out of which we shall focus on time-distance seismology (Duvall Jr. et al., 1993). This approach lets us relate travel-time shifts of seismic waves in the sun to surface and sub-surface velocities, thereby setting up

an inverse problem where measurements of wave travel-times can be used to estimate flow fields in the solar interior. Time-distance seismology has been widely used to recover flows in the Sun (Duvall & Gizon, 2000; Zhao & Kosovichev, 2003; Zhao, 2004; Jackiewicz et al., 2008; Duvall & Hanasoge, 2012; Švanda, 2012), however when applied specifically to supergranules, the sub-surface flow profiles have been hard to pin down.

Despite successful measurements of supergranular flows on the solar surface (Rieutord et al., 2008; Duvall & Birch, 2010; Švanda et al., 2013), seismic studies have not been successful at consistently reproducing the sub-surface profiles of supergranules. Duvall (1998) used correlations between inverted surface and deeper flows to determine the lower bound of the supergranule pattern where the convective cell overturns, and obtained a depth of 8 Mm. Zhao & Kosovichev (2003) used time-distance seismology to invert MDI data and inferred that the depth of a supergranule was 15 Mm. Braun et al. (2004) applied phase-sensitive holography to MDI data and concluded that detection of return flow below 10 Mm

would prove to be a significant challenge due to contamination from neighboring supergranules. Woodard (2007) used Fourier-space correlations in the observed wave field, and found power to extend down to 6 Mm below the surface before noise took over; similar results were also obtained by Braun et al. (2007) using helioseismic holography and Jackiewicz et al. (2008) using time-distance seismology. Using measurements of horizontal flow divergences and vertical velocity obtained from Solar Optical Telescope (SOT) on board the Hinode satellite, Rieutord et al. (2010) estimated the vertical scale height of supergranules to be 1 Mm. Duvall & Hanasoge (2012) used a ray-theoretic forward modeling approach to fit center-annulus travel-time differences obtained using Gaussian models of vertical velocity to those obtained from a kinematic model of an “averaged supergranule” derived using Dopplergrams from Helioseismic and Magnetic Imager (HMI; Schou et al., 2012) on-board the Solar Dynamics Observatory (SDO) spacecraft. They estimated that the depth corresponding to peak vertical velocity to be  $2.3 \pm 0.9$  Mm, where the value signified by  $\pm$  represents the width of the model. Additional evidence for a shallow supergranule was obtained by Duvall et al. (2014).

The prevalence of disparate values and the dependence of results on the specific technique being used calls for validation tests of seismic inversion algorithms. Dombroski et al. (2013) tested regularized least square inversions using helioseismic holography measurements for a supergranulation-like flow, but found that the inferred vertical flow has significant errors throughout the computational domain. Švanda et al. (2011) used subtractive optimally localized averages (SOLA) (Jackiewicz et al., 2008) and were able to recover 3-dimensional velocity fields from forward-modeled travel-time maps generated from simulations of solar-like convective flows. However Švanda (2015) showed that reconstructed velocity fields do not produce wave travel times that match the observed ones. DeGrave et al. (2014) tried validating time-distance SOLA inversions using realistic solar simulations, and found that they could recover horizontal flows till 5 Mm below the solar surface, but were unable to infer vertical flows accurately like Švanda et al. (2011). The authors attributed this to differences in measurement and analysis techniques. A different approach was tried by Hanasoge (2014) and Bhattacharya & Hanasoge (2016), who used full-waveform inversion (Tromp et al., 2010) to iteratively update a Cartesian 2-dimensional flow profile to minimize travel-times misfit computed with respect to a model similar to the average supergranule from Duvall & Birch (2010). They found that seismic waves in their simulations were primarily sensitive to flow updates close to the solar surface, and inversions focused on updating these layers at the expense of deeper layers. This negative result — especially for a noise-free inver-

sion — was surprising in light of the previous studies by Švanda et al. (2011) and DeGrave et al. (2014), and urged one to probe deeper into the reasons behind this mismatch.

In this work we follow an approach similar to Bhattacharya & Hanasoge (2016), but ask an important question — can we pose the problem differently to avoid the interplay between the large number of parameters being inverted for, and reduce the question to the fundamental one of seismic sensitivity to flows? The means by which we approach the question is to consider the pedagogic exercise of inverting for a 2-dimensional section of the averaged supergranule of Duvall & Hanasoge (2012), using seismic waves that are excited by sources located at specific spatial locations. While the setup is not directly comparable with solar observations, this serves as a computationally efficient starting point to validate full-waveform inversion applied to the Sun. We project the supergranular flow model in a B-spline basis and solve an optimization problem to obtain the spline coefficients. We show that we are able to accurately recover the vertical profile of the averaged supergranule down to 8 – 10 Mm below the surface. This result might help to guide the construction of improved inversion strategies to study the subsurface profile of an averaged supergranule in the Sun.

## 2. Supergranule model

We consider kinematic models of temporally stationary supergranules in Cartesian coordinates. The entire analysis is two-dimensional primarily for computational ease, although it provides us with an extra simplification that would be absent in three dimensions — that of a unidirectional stream function. We choose coordinates  $\mathbf{x} = (x, z)$ , where  $z$  is a vertical coordinate that increases in the direction opposite to gravity, and  $x$  denotes a horizontal direction with periodic boundary conditions. We set  $z = 0$  at the solar surface, therefore negative values of  $z$  indicate depths below and positive values indicate heights above it.

A model of a supergranule can be described by its velocity field  $\mathbf{v}(\mathbf{x})$  that is embedded in a steady solar background characterized by a one-dimensional density profile  $\rho(z)$ , sound-speed profile  $c(z)$ , pressure  $p(z)$ , acceleration due to gravity  $\mathbf{g}(z) = -g(z) \mathbf{e}_z$ . The velocity profile of the supergranule is chosen to resemble a section through the averaged supergranule of Duvall & Hanasoge (2012), differences arising because of the computation being in Cartesian coordinates rather than cylindrical.

We enforce mass-conservation

$$\nabla \cdot (\rho \mathbf{v}) = 0, \quad (1)$$

and derive the velocity field from a stream function  $\psi(\mathbf{x}) \mathbf{e}_y$  as

$$\mathbf{v} = \frac{1}{\rho} \nabla \times [\rho c \psi \mathbf{e}_y]. \quad (2)$$

Our model for the supergranule stream function is

$$\psi(\mathbf{x}) = \frac{v_0}{c(z)} \frac{\text{sign}(x)}{k} J_1(k|x|) \exp\left(-\frac{|x|}{R}\right) \times \exp\left(-\frac{(z-z_0)^2}{2\sigma_z^2}\right), \quad (3)$$

where  $J_1$  is the Bessel function of order 1. The supergranule stream function is zero at the cell center, peaks at a certain distance away from the center before falling to zero and reversing sign; the reversal in sign indicates a transition in the vertical velocity from upflows to downflows. The model is highly simplified compared to supergranules as observed on the solar surface, as it ignores the impact of magnetic fields and other observed anomalous characteristics such as wave-like nature associated with supergranules (Gizon et al., 2003) and east-west travel-time asymmetries (Langfellner et al., 2015). We fix the horizontal length scales to  $R = 15$  Mm and  $k = 2\pi/(30 \text{ Mm})$ , and use several combinations of parameters to characterize the vertical profile. These parameters are listed in Table 1.

The flow field that we obtain from this stream function is

$$v_x = v_0 \frac{\text{sign}(x)}{k} J_1(k|x|) \exp\left(-\frac{|x|}{R}\right) \times \left(\frac{(z-z_0)}{\sigma_z^2} - \frac{\rho'(z)}{\rho(z)}\right) \exp\left(-\frac{(z-z_0)^2}{2\sigma_z^2}\right), \quad (4)$$

$$v_z = v_0 \left(\frac{1}{2} (J_0(k|x|) - J_2(k|x|)) - \frac{1}{kR} J_1(k|x|)\right) \times \exp\left(-\frac{|x|}{R}\right) \exp\left(-\frac{(z-z_0)^2}{2\sigma_z^2}\right). \quad (5)$$

We list the magnitude of the peak and surface velocities for these flow fields in Table 2. In subsequent analysis, we shall refer to this velocity field with the superscript “true”, ie. as  $\mathbf{v}^{\text{true}}$ , and similarly for its components, to distinguish it from the flow velocity in the iteratively updated flow model. We shall apply superscripts “true” and “iter” to other parameters wherever necessary, indicating which model they correspond to.

### 3. Inversion Setup

Waves in the Sun are driven near the solar surface by turbulent convection associated with granules, with most of the excitation taking place within 500 km of the photosphere (Stein & Nordlund, 2001). Once generated, seismic waves propagate under the restoring forces applied

**Table 1.** Stream-function parameters

Model	$z_0$ [Mm]	$\sigma$ [Mm]	$v_0$ [m/s]
SG1	-2.3	0.9	240
SG2	-4	1.6	270
SG3	-6	2.2	600
SG4	-8	2.8	700

by fluid pressure gradients and gravity. The wave displacement  $\xi(\mathbf{x}, t)$  evolves according to the equation

$$\rho \partial_t^2 \xi + 2\rho \mathbf{v} \cdot \nabla \partial_t \xi = \nabla (c^2 \rho \nabla \cdot \xi + \xi \cdot \nabla p) + \mathbf{g} \nabla \cdot (\rho \xi) + \mathbf{S}, \quad (6)$$

where  $\mathbf{S}$  represents sources that are exciting waves in the Sun. In our simulation, we choose eight sources located at different horizontal positions at a depth of 150 km below the surface. The sources represent “master pixels” (Tromp et al., 2010; Hanasoge et al., 2011), that is their locations are chosen so that the emanating waves sample the supergranule adequately. Each source fires independent of the others, and produces waves that illuminate slightly different regions in the Sun. For both the true supergranule and the iterated one, therefore, we have eight different simulations that are computed in parallel, each of which runs for 4 hours in solar time. The simulation box spans 800 Mm horizontally over 512 pixels, and extending from 137 Mm below the surface to 1.18 Mm above it vertically, resolved using 300 pixels spaced uniformly in acoustic distance. We place perfectly matched layers along the vertical boundaries to absorb waves effectively.

We use the seismic wave propagation code SPARC (Hanasoge & Duvall, 2007) to solve the wave equation in a convectively stabilized version of Model S (Christensen-Dalsgaard et al., 1996). The model is one-dimensional and satisfies hydrostatic balance, and is stabilized by patching an isothermal layer to Model S above  $0.98 R_\odot$  (Hanasoge et al., 2006). The code SPARC computes seismic wave fields by solving Equation (6) in the time domain using a low-dispersion and low-dissipation five-stage Runge-Kutta time-stepping scheme (Hu et al., 1996). Spatial derivatives are computed using a sixth-order compact finite-difference scheme (Lele, 1992) in the vertical direction, and using Fourier decomposition in the horizontal direction.

We apply ridge-filters to study the propagation of wavepackets corresponding to individual radial orders. The ideal filtering technique has been a subject of some debate: it was found by Svanda (2013) that inversions using a ridge-filtered approach produces results consistent with one using a phase-speed filtered approach, while DeGrave et al. (2014) found that inversions using ridge-filtered travel times do not compare favorably with

**Table 2.** Peak velocities, surface velocities and depths for the four models considered.

Model	Max $v_x$ [m/s]	Max $v_x$ at surface [m/s]	$v_x$ peak depth [Mm]	Max $v_z$ [m/s]	Max $v_z$ at surface [m/s]	$v_z$ peak depth [Mm]
SG1	601	222	1.4	111	5	2.3
SG2	390	245	2.7	128	6	3.9
SG3	614	293	4.2	284	7	6.1
SG4	539	228	5.2	333	6	8.1

**Table 3.** Source-receiver distances

Radial Order	Receiver Distance [Mm]
$f$	12 – 100
$p_1$	12 – 120
$p_2$	12 – 150
$p_3$	12 – 200
$p_4$	12 – 250

phase-speed-filtered ones, however we do not address this issue in the present work. Following Jackiewicz et al. (2008), we filter the data by multiplying the wave spectrum by a function of the form  $F_n(\nu, k)$ , where  $\nu$  represents temporal frequency,  $k$  represents spatial frequency and  $n$  represents the radial order. The filter function is constructed by separating modes corresponding to different radial orders using fourth-order polynomials of  $k$ . For each radial order, the spectral area enclosed between two such polynomials  $\nu_{low}(k)$  and  $\nu_{high}(k)$  is entirely included. We list the polynomials used for each radial order in Table 3. The selected temporal-frequency band at each pixel in  $k$  is terminated with a quarter of a cosine function over two pixels on both the high and low edges to ensure a smooth fall-off. Additionally low temporal frequency modes below 1.1 mHz are filtered out to remove contributions from weak  $g$ -modes that arise as an artifact of the convectively stabilized background.

We choose a group of pixels 200 km above the surface and mark them as receivers. We list the horizontal locations of receivers for various radial orders in Table 3. The wide range of receiver locations combines both short and large-distance measurements, thereby utilizing waves that probe various depths beneath the solar surface. We record filtered waveforms with time for  $f$ ,  $p_1$ ,  $p_2$  and  $p_3$  ridges at each receiver pixel for each simulation, and for the  $p_4$  ridge as well for the case of SG4. An example of a spectrum along with a filter to extract waves corresponding to the radial order  $p_2$ , as well as measured travel-times at receivers for the model SG2 is

depicted in Fig 1. We define the travel-time misfit

$$\chi = \frac{1}{2} \sum_s \sum_{\text{ridge}} \sum_r (\tau_{s,r,\text{ridge}}^{\text{true}} - \tau_{s,r,\text{ridge}}^{\text{iter}})^2, \quad (7)$$

where  $\tau_{s,r,\text{ridge}}^{\text{true}}$  refers to the waves emanating from the source  $s$  whose ridge-filtered travel-time is measured at the  $r$ -th receiver in presence of the true supergranule,  $\tau_{s,r,\text{ridge}}^{\text{iter}}$  is the travel-time measured in presence of the iterated model for the same source-receiver locations and the same filter, and the sum extends over source-receiver pairs as well as different radial orders. We compute travel-times in a manner similar to Gizon & Birch (2002), we describe the technique in detail in Appendix A.

Non-linear iterative time-distance inversions, as formulated in the context of helioseismology by Hanasoge (2014), revolves around reducing the misfit defined in Equation (7) by sequentially improving a model of the supergranule. The scheme proceeds by relating the travel-time misfit to an update in the supergranule stream function through an integral relation as

$$\delta\chi = \int_{\odot} d\mathbf{x} K_{\psi}(\mathbf{x}) \delta\psi(\mathbf{x}), \quad (8)$$

where  $K_{\psi}(\mathbf{x})$  is the kernel whose value at any spatial point indicates sensitivity of wave travel-times to local updates  $\delta\psi(\mathbf{x})$  in the supergranule model. We use the adjoint source technique (Hanasoge et al., 2011) to compute the finite-frequency kernel  $K_{\psi}(\mathbf{x})$ . The steps involved in computing this kernel have been detailed in Hanasoge (2014) and Bhattacharya & Hanasoge (2016).

### 3.1. Basis-resolved Inversion

Previous attempts at inversions by Hanasoge (2014) and Bhattacharya & Hanasoge (2016) have focused on solving for the stream function at each spatial location. The number of parameters being inverted for was equal to the number of spatial grid points, ie. for a  $512 \times 300$  grid we would have had 153600 parameters. One of the questions we ask in this paper is whether the large size of the parameter space had kept the previous attempts from converging to the correct model. To answer this question, we pose the inverse problem differently and make the following assumptions:

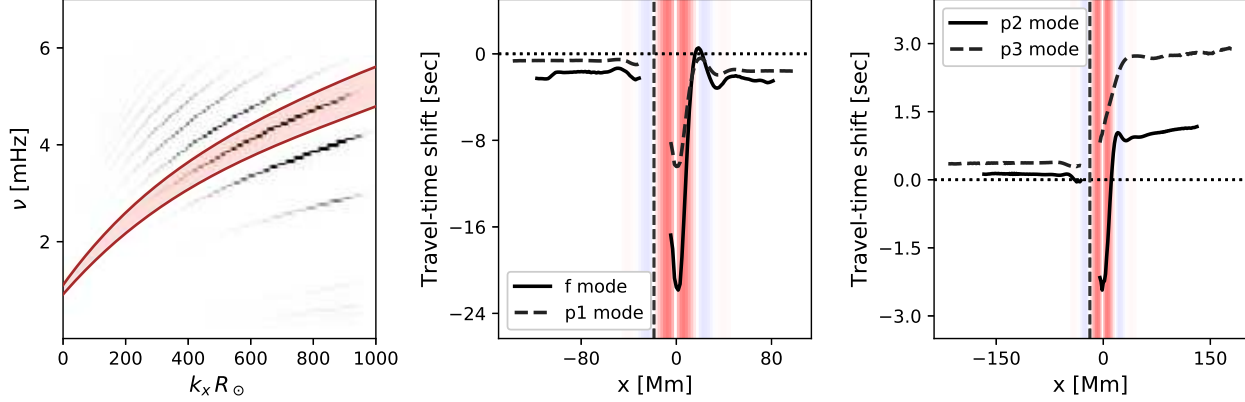


**Figure 1.** Left panel: Wave spectrum overlain with the function used to filter waves corresponding to the radial order  $p_2$ . Middle and right panels: Travel-time shifts between waves in the starting and true flow models for supergranule SG2, computed at all receivers for different radial orders. The horizontal location of the source is marked by the dashed vertical line. The horizontal flow field of the supergranule is indicated by the colored patch in the background, where red indicates outflows away from the cell center, and blue indicates inflows towards the cell center.

1. The supergranule stream function is separable in  $x$  and  $z$ . This assumption is made keeping in mind that we are primarily interested in the depth of supergranules.
2. The value of the stream function at the surface and above is known. The justification is that the layers at and above the surface are directly observed, and hence the flow velocities measured. (Gizon et al., 2000; Rieutord et al., 2008; Duvall & Birch, 2010)

A consequence is that the horizontal profile of the stream function is assumed to be known everywhere, and we only solve for its vertical profile. We express the stream function as

$$\psi^{\text{iter}}(\mathbf{x}) = f(x) g^{\text{iter}}(z), \quad (9)$$

where  $f(x)$  is entirely determined, and  $g^{\text{iter}}(z)$  is known for  $z > 0$ . We represent the true model for the stream function from Equation (3) in a similar manner as  $\psi^{\text{true}}(\mathbf{x}) = f(x) g^{\text{true}}(z)$ , where  $g^{\text{true}}(z)$  is the function that we seek to recover through the inversion.

We reduce the parameter space further by expanding the vertical profile of  $\psi^{\text{true}}(\mathbf{x})$  in a basis of B-splines and inverting for the coefficients close to the surface. We expand the vertical profile  $g^{\text{true}}(z)$  in a basis of quadratic B-splines with a given set of knots  $\{t\}$  as

$$g^{\text{true}}(z) \approx \sum_{i=0}^{N-1} \beta_i^{\text{true}} B_i(z; t, k=2), \quad (10)$$

where  $\beta_i$  represent the B-spline coefficients, and  $k=2$  indicates quadratic splines. The B-splines are ordered such that the index  $i=0$  corresponds to the B-spline function that peaks the deepest, while the index  $i=N-1$  corresponds to the one that peaks close to the upper boundary

of our computational domain. The approximate equality is to be understood as the best fit in a least-square sense, since we choose a set of smoothing splines instead of interpolating ones. We describe the spline expansion in detail in Appendix B. We would like to point out that such an approach is applicable only to an ensemble averaged model of a supergranule, where the flow profile is expected to be smooth and representable using relatively few splines.

We split the coefficients into two groups — those above the surface and those below the surface. Assuming that the coefficient with index  $m$  corresponds to the B-spline function that peaks at the solar surface, we rewrite Equation (10) as

$$\begin{aligned} g^{\text{true}}(z) &\approx \sum_{i=0}^{m-1} \beta_i^{\text{true}} B_i(z; t, k=2) \\ &+ \sum_{i=m}^{N-1} \beta_i^{\text{true}} B_i(z; t, k=2) \\ &= \sum_{i=0}^{m-1} \beta_i^{\text{true}} B_i(z; t, k=2) + g^{\text{surf}}(z). \end{aligned} \quad (11)$$

We choose the surface profile  $g^{\text{surf}}(z)$  and use Equation (9) to obtain the starting model of our supergranule, ie

$$\psi^{\text{start}}(\mathbf{x}) = f(x) g^{\text{surf}}(z). \quad (12)$$

The starting flow profile in our inversion is the same as the true flow above the surface, and falls to zero continuously just below. We can represent the vertical profile of the starting supergranule stream function in a basis of

splines by setting the coefficients of B-splines below the surface to zero, ie.

$$g^{\text{surf}}(z) = \sum_{i=0}^{N-1} \beta_i^{\text{start}} B_i(z; t, k=2), \quad (13)$$

$$\beta_i^{\text{start}} = \begin{cases} 0 & i < m \\ \beta_i^{\text{true}} & i \geq m \end{cases}. \quad (14)$$

This is the model that we shall iteratively update, therefore at the first step of the inversion we set  $\psi^{\text{iter}} = \psi^{\text{start}}$ , or equivalently  $\beta_i^{\text{iter}} = \beta_i^{\text{start}} \forall i$ . This choice is different from that made by Hanasoge (2014) and Bhattacharya & Hanasoge (2016), where the starting model had no flows. Note that we use the same set of knots  $\{t\}$  to represent the inverted model as the ones that we had used to expand  $g^{\text{true}}(z)$  in Equation (10). The inversion is carried out to obtain the spline coefficients  $\{\beta_i^{\text{iter}}\}$  that lie below the solar surface.

We substitute the spline expansion of the iterated stream function in Equation (8) to obtain kernels in spline space as

$$\begin{aligned} \delta\chi &= \sum_{i=0}^{m-1} \left[ \int_{\odot} d\mathbf{x} K_{\psi}(\mathbf{x}) f(x) B_i(z; t, k=2) \right] \delta\beta_i^{\text{iter}} \\ &= \sum_{i=0}^{m-1} K_i \delta\beta_i^{\text{iter}}. \end{aligned} \quad (15)$$

The discrete kernels  $K_i$  indicate the sensitivity of travel-times to individual B-spline coefficients. We use the Broyden–Fletcher–Goldfarb–Shanno algorithm (BFGS, Nocedal & Wright, 2006) to iteratively update our model of the supergranule flow profile and reduce the travel-time misfit.

### 3.2. Regularization

The simulated spectrum (left panel in Figure 1) features discernible modal ridges from  $f$  to  $p_6$ , out of which we use ridges up to  $p_4$  for our study. Restricting ourselves to a small set of modes imposes a limit on the depth until which we can infer flows, beyond this waves have limited sensitivity to flows. We therefore compute the knots required for the basis expansion in Equation (10) with a lower cutoff imposed. The depth of the cutoff is governed by the modes used in the inversion for each model, but it is chosen to be deep enough to ensure that the entire flow profile is contained within the spatial range.

We can estimate the depths that seismic waves probe by computing the asymptotic lower turning point (Giles, 2000). The turning-point for a wave that has the maximum power in the  $p_3$  ridge — corresponding to  $k_x R_{\odot} = 533$  and temporal frequency  $\nu = 4.5$  mHz in the simulation — is 9 Mm. We therefore expect inferences using radial orders  $f - p_3$  to be accurate down to this

depth. This also indicates that waves from the  $p_4$  and higher radial orders might be necessary to infer flows deeper down. The value of lower cutoff and number of spline coefficients used for each model is listed in Table B.1 in Appendix B. We ensure that the iterated flow model falls smoothly to zero at the lower cutoff by multiplying the  $i^{\text{th}}$  B-spline coefficient by a factor of  $1/(1 + \exp(-(i - i_2)/0.2))$ , where  $i_2$  is the index of the coefficient that lies 2 Mm above the lower cutoff. For models SG1, SG2 and SG3 we obtain  $i_2 = 1$ , indicating that the two deepest coefficients ( $i = 0$  and  $i = 1$ ) are suppressed by factors of 150 and 2 respectively, whereas for SG4 we obtain  $i_2 = 0$ , indicating that the value of the deepest coefficient ( $i = 0$ ) is reduced by a factor of 2.

Previous analysis by Bhattacharya & Hanasoge (2016) had used spatial smoothing to reduce high spatial-frequency variation in the numerically computed sensitivity kernel. This is not strictly necessary in our approach, and we found minor differences by including smoothing.

## 4. Results and discussion

The “inversion” in our analysis is a series of forward simulations, followed by optimization in the parameter space of the flow. Each stage in the iterative optimization proceeds by reducing the travel-time misfit in Equation (7). We plot the travel-time for different radial orders for the model SG2 in Figure 1. We compare the travel-time shift with the horizontal flow that is indicated by the colored patch. The travel-time shift is a measure how much the waveform in the starting model is delayed with respect to that in the true model, negative values indicating that the wavepacket in the starting model arrives earlier at a receiver in relation to the true model.

Each model is updated by iteratively reducing the travel-time misfit using Equation (8). In solar travel-time measurements, error bars arising from realization noise provide a natural stopping point for iterations; in the absence of noise we iterate until the relative change in travel-misfit falls below 0.1%. We quantify the efficacy of the inversion by defining model misfits for the stream function and the components of the flow. The flow velocities are related to derivatives of stream function through Equation (2), so the misfit in components of flow, when computed at each depth, differs from that for the stream function. The misfit  $\kappa$  for each parameter is defined as the normalized square of the difference between true and iterated models evaluated as a function of depth by averaging over the horizontal direction  $x$ , ie. for the stream function  $\psi$  we obtain

$$\kappa[\psi](z) = \frac{\int dx (\psi^{\text{true}}(x, z) - \psi^{\text{iter}}(x, z))^2}{\int dx \psi^{\text{true}}(x, z = \text{argmax}_z g^{\text{true}}(z))^2}, \quad (16)$$

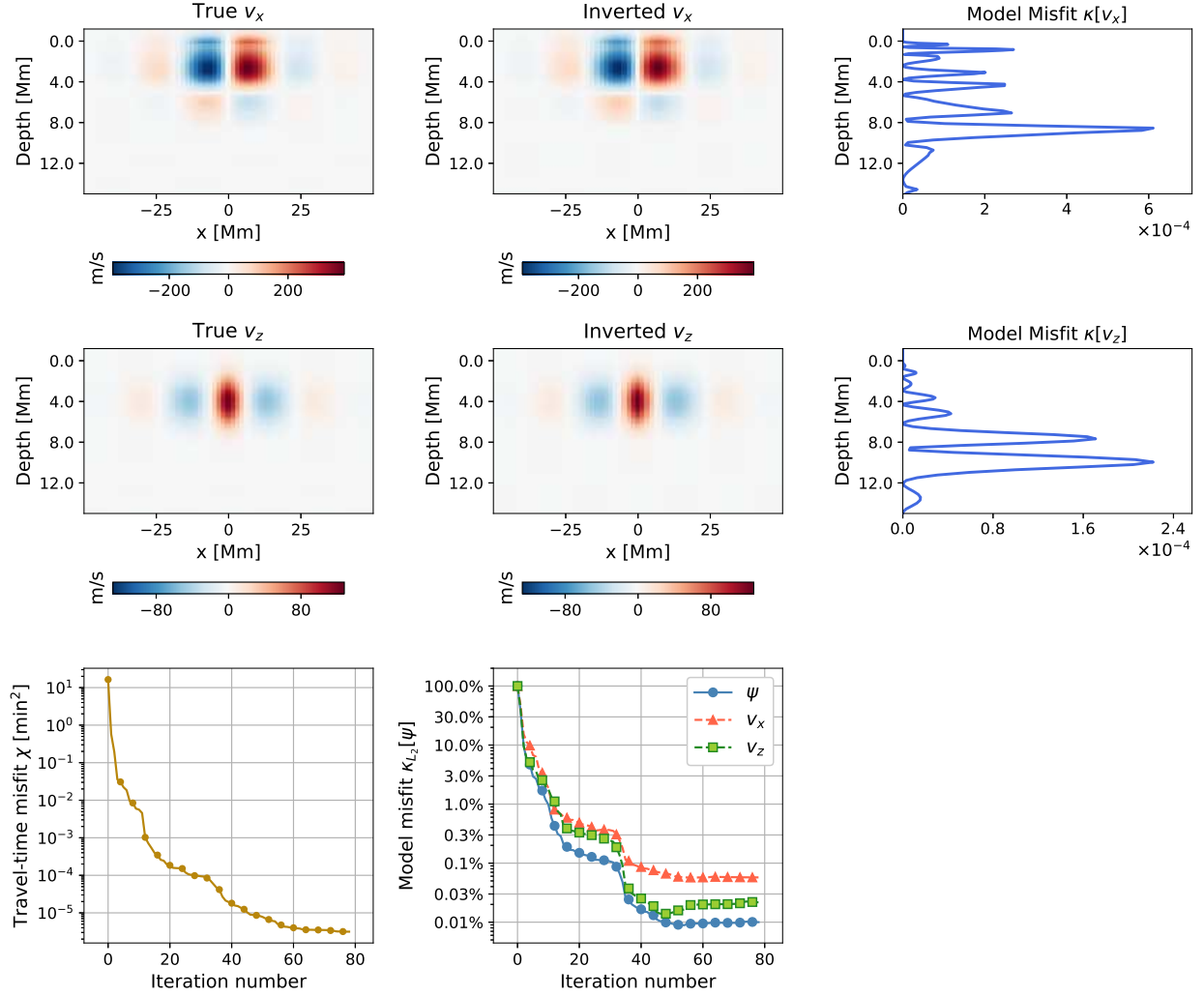


**Figure 2.** True and inverted flow velocity for SG2 from Table 1, with data and model misfits. The panels are — top left: true  $v_x$ , top center: inverted  $v_x$ , top right: misfit in  $v_x$  as a function of depth (Equation 18), middle left: true  $v_z$ , middle center: inverted  $v_z$ , middle right: misfit in  $v_z$  as a function of depth (Equation 19), bottom left: data misfit from Equation (7), bottom center: model misfit from Equation (20) for the stream function  $\psi$  and the two components of velocity. We see that the inverted flow matches the true flow reasonably well, with the vertical profiles differing by less than 0.5%.

where the horizontal integral in the denominator is evaluated at the depth where the true model reaches its peak. This ensures that the maximum misfit for the starting model is normalized to one. The notation here indicates that the misfit  $\kappa$  is computed for the parameter in square brackets, and is evaluated as a function of vertical layer  $z$ . Using the separability condition in Equation (9), we can express  $\kappa[\psi]$  in term of the vertical profile  $g(z)$  as

$$\kappa[\psi](z) = \frac{(g^{\text{true}}(z) - g^{\text{iter}}(z))^2}{[\max g^{\text{true}}(z)]^2}. \quad (17)$$

We define analogous misfit functions for the two components of flow velocity, the expressions being

$$\kappa[v_x](z) = \frac{\left[ \frac{1}{\rho} \partial_z (\rho c (g^{\text{true}}(z) - g^{\text{iter}}(z))) \right]^2}{\left[ \max \left( \frac{1}{\rho} \partial_z (\rho c g^{\text{true}}(z)) \right) \right]^2}. \quad (18)$$

$$\kappa[v_z](z) = \frac{c^2 (g^{\text{true}}(z) - g^{\text{iter}}(z))^2}{[\max (c g^{\text{true}}(z))]^2}. \quad (19)$$

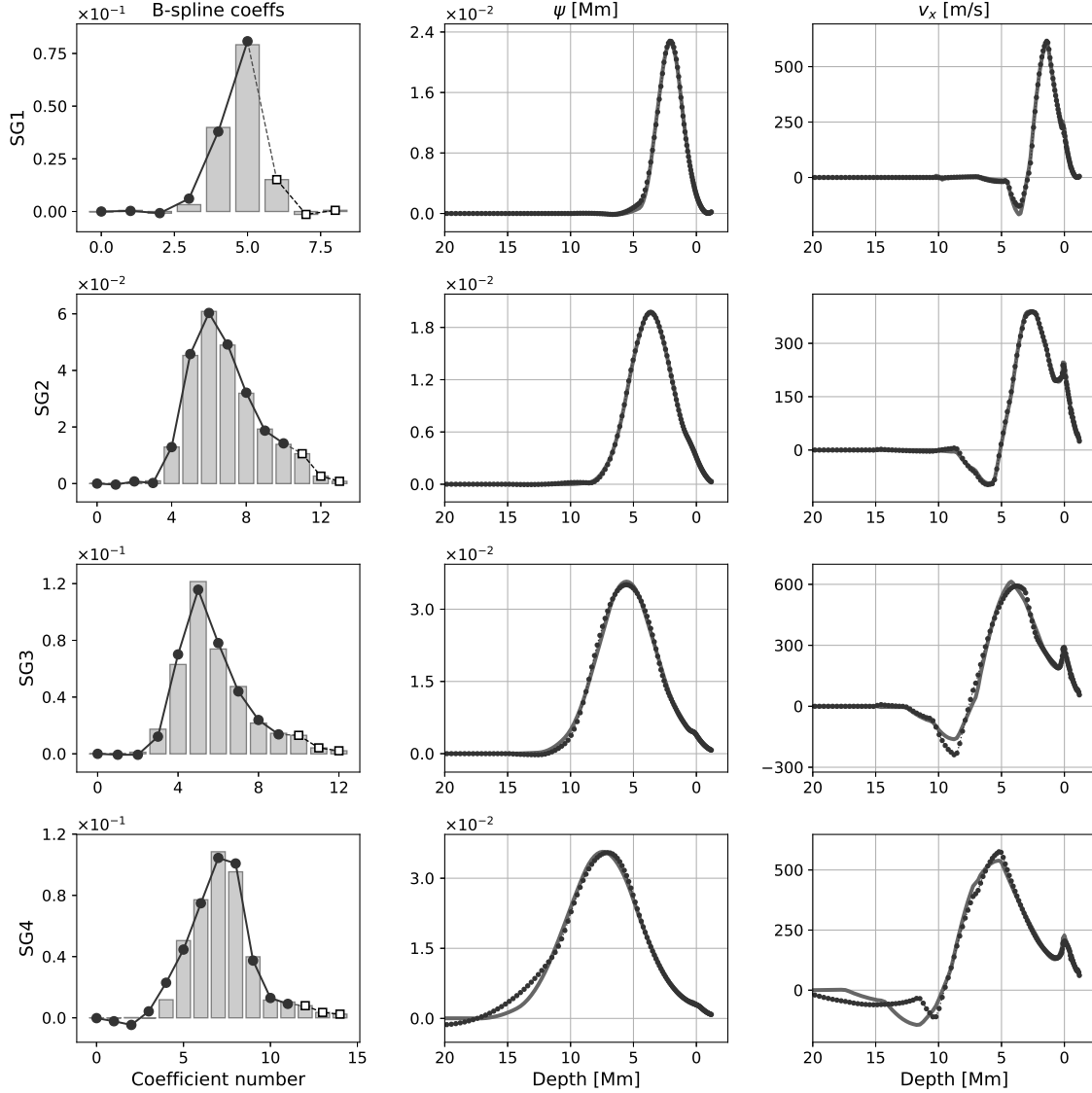


**Figure 3.** True and inverted profiles for the four supergranule Gaussian profiles from Table 1. Each row corresponds to one model, with the left panel representing the B-spline coefficients, the middle panel showing the vertical profile of the stream function, and the rightmost panel depicting the vertical profile of the horizontal component of the flow velocity. The profile of vertical flow is not plotted, but is similar to the stream function. In the leftmost panel for each row, bars represent B-spline coefficients for the true stream function, white squares represent spline coefficients above the surface — these are clamped to the value in the true model — while black circles represent spline coefficients for the inverted solution. In the middle and right panels of each row, gray solid lines represents vertical profiles of the true models, and black circles denote the profile for the inversion result. We find that stream functions are reasonably well matched down to a depth of 10 Mm from the surface, as expected for an inversion using  $f - p_3$  modes. The magnitude of horizontal return flow, however, is captured correctly only the relatively shallower models SG1 and SG2.

Alongside studying misfit as a function of depth, we consider the normalized  $L_2$  norm of differences between true and iterated models integrated over the entire space,

defined as

$$\kappa_{L_2}[\psi](z) = \frac{\int dz (g^{\text{true}}(z) - g^{\text{iter}}(z))^2}{\int dz (g^{\text{true}}(z) - g^{\text{start}}(z))^2}, \quad (20)$$



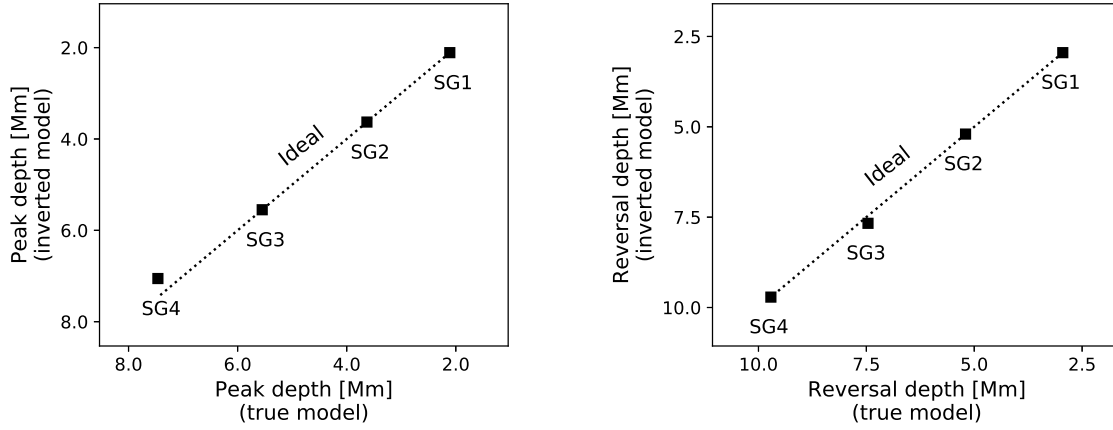


**Figure 4.** Left: Peak depths of the inverted stream function versus that of the true model, for each of the different supergranules from Table 1. The dotted line indicates the ideal recovered peak depth, ie. that of the true model. Right: Reversal depths of  $v_x$  in the inverted models against those in the true ones. The depth of reversal is one indicator of the vertical extent of a supergranule (Duvall, 1998).

to gain insight into the degree of improvement to the model after each iteration. We compare the inverted flow velocity field with the profile of the model SG2 in Figure 2, and analyze the model misfit. We find that the inversion result matches the true model reasonably well, with the stream function misfit  $\kappa_{L_2}[\psi]$  being around 0.01% after the final iteration.

We plot the inverted vertical profiles of all the models in Figure 3. One question we ask in this paper is whether seismic waves can estimate the depth of supergranules. We plot the expected and inferred peak depths for each model in Figure 4. We find that we recover the peak depths accurately for all the models. It is encouraging to note that we are able to extract Gaussian profiles up to a depth of 8 – 10 Mm, that is beyond the 6 Mm limit found by previous seismic inferences in the presence of realization noise (Braun et al., 2007; Woodard, 2007). We were however unable to retrieve the profile for a deeper model with a peak depth of 14 Mm with  $f - p_4$  modes. It might be interesting to see if the introduction of higher  $p$  modes makes a difference.

Aside from peak depth, another important parameter that is used to estimate supergranules depth is the layer at which the horizontal flow reverses direction. All the models that we study have a reversal in  $v_x$ , keeping with the assumption of a steady convective cell. We compare the true and inferred reversal depths in Figure 4. We find that the inversion reproduces comparable values, although the exact profile of the return flow is not accurately captured. Whether the reversal actually takes place is subject to debate, since it is not detected in the study by Woodard (2007) and suggested to be spurious by Švanda (2013); DeGrave et al. (2014). Our results seem to indicate that the depth would be captured

correctly for shallow models if the flow does reverse, provided the inference is not limited by noise.

In this work we have used iterative forward modeling to obtain the best-fit flow model given travel-time measurements at the solar surface. This approach is inherently non-linear, as it requires re-computing the sensitivity kernel after each iteration. From Figure 2, we see that a substantial drop in model misfit takes place in the first few iterations. This makes it interesting to compare this approach with a linear inversion; given the small parameter space, it might be possible to pinpoint the differences in the inverted flow arising from the two approaches. We have also not considered any noise associated with travel-time measurements, so this analysis can not be directly applied to solar measurements. It would be interesting to study the extent to which the inferences are affected in presence of noise, and develop a slightly modified technique that accounts for realistic noise covariance matrices (Gizon & Birch, 2004; Švanda et al., 2011). It was also pointed out by DeGrave et al. (2014) that validation tests with frozen non-magnetic flow fields might be too idealized a scenario compared to studying a Doppler time-series obtained from the Sun. Therefore an extension of this work to flows present in realistic solar simulations might be in order.

*Acknowledgements.* SMH acknowledges support from Ramanujan fellowship SB/S2/RJN-73/2013, the Max-Planck partner group program and thanks the Center for Space Science, New York University at Abu Dhabi. JB acknowledges the financial support provided by the Department of Atomic Energy, India.

## References

Bhattacharya, J. & Hanasoge, S. M. 2016, ApJ, 826, 105

- Braun, D. C., Birch, A. C., Benson, D., Stein, R. F., & Nordlund, Å. 2007, *ApJ*, 669, 1395
- Braun, D. C., Birch, A. C., & Lindsey, C. 2004, in *ESA Special Publication*, Vol. 559, SOHO 14 Helio- and Asteroseismology: Towards a Golden Future, ed. D. Danesy, 337
- Christensen-Dalsgaard, J., Dappen, W., Ajukov, S. V., et al. 1996, *Science*, 272, 1286
- DeGrave, K., Jackiewicz, J., & Rempel, M. 2014, *ApJ*, 788, 127
- Dierckx, P. 1993, *Curve and Surface Fitting with Splines* (New York, NY, USA: Oxford University Press, Inc.)
- Dombroski, D. E., Birch, A. C., Braun, D. C., & Hanasoge, S. M. 2013, *Solar Physics*, 282, 361
- Duvall, J. & Birch, A. C. 2010, *ApJ*, 725, L47
- Duvall, T. & Hanasoge, S. 2012, *Sol. Phys.*, 136
- Duvall, T. L., Hanasoge, S. M., & Chakraborty, S. 2014, *Sol. Phys.*, 289, 3421
- Duvall, Jr., T. L. 1998, in *ESA Special Publication*, Vol. 418, *Structure and Dynamics of the Interior of the Sun and Sun-like Stars*, ed. S. Korzennik, 581
- Duvall, Jr., T. L. & Gizon, L. 2000, *Sol. Phys.*, 192, 177
- Duvall Jr., T., Jefferies, S., Harvey, J., & Pomerantz, M. 1993, *Nature*, 362, 430
- Giles, P. M. 2000, PhD thesis, STANFORD UNIVERSITY
- Gizon, L. & Birch, A. C. 2002, *ApJ*, 571, 966
- Gizon, L. & Birch, A. C. 2004, *ApJ*, 614, 472
- Gizon, L., Birch, A. C., & Spruit, H. C. 2010, *ARA&A*, 48, 289
- Gizon, L., Duvall, T. L., & Schou, J. 2003, *Nature*, 421, 43
- Gizon, L., Duvall, Jr., T. L., & Larsen, R. M. 2000, *Journal of Astrophysics and Astronomy*, 21, 339
- Hanasoge, S. M. 2014, *ApJ*, 797, 23
- Hanasoge, S. M., Birch, A., Gizon, L., & Tromp, J. 2011, *ApJ*, 738, 100
- Hanasoge, S. M. & Duvall, Jr., T. L. 2007, *Astronomische Nachrichten*, 328, 319
- Hanasoge, S. M., Larsen, R. M., Duvall, Jr., T. L., et al. 2006, *ApJ*, 648, 1268
- Hathaway, D. H., Beck, J. G., Bogart, R. S., et al. 2000, *Sol. Phys.*, 193, 299
- Hu, F. Q., Hussaini, M. Y., & Manthey, J. L. 1996, *Journal of Computational Physics*, 124, 177
- Jackiewicz, J., Gizon, L., & Birch, A. C. 2008, *Sol. Phys.*, 251, 381
- Jackiewicz, J., Gizon, L., Birch, A. C., & Duvall, Jr., T. L. 2007, *ApJ*, 671, 1051
- Langfellner, J., Gizon, L., & Birch, A. C. 2015, *A&A*, 579, L7
- Lele, S. K. 1992, *Journal of Computational Physics*, 103, 16
- Nocedal, J. & Wright, S. J. 2006, *Numerical Optimization*, 2nd edn. (New York: Springer)
- Nordlund, Å., Stein, R. F., & Asplund, M. 2009, *Living Reviews in Solar Physics*, 6, 2
- Rieutord, M., Meunier, N., Roudier, T., et al. 2008, *A&A*, 479, L17
- Rieutord, M., Roudier, T., Rincon, F., et al. 2010, *A&A*, 512, A4
- Schou, J., Scherrer, P. H., Bush, R. I., et al. 2012, *Sol. Phys.*, 275, 229
- Stein, R. F. & Nordlund, Å. 2001, *ApJ*, 546, 585
- Tromp, J., Luo, Y., Hanasoge, S., & Peter, D. 2010, *Geophysical Journal International*, 183, 791
- Švanda, M. 2012, *ApJ*, 759, L29
- Švanda, M. 2013, *ApJ*, 775, 7
- Švanda, M. 2015, *A&A*, 575, A122
- Švanda, M., Gizon, L., Hanasoge, S. M., & Ustyugov, S. D. 2011, *A&A*, 530, A148
- Švanda, M., Roudier, T., Rieutord, M., Burston, R., & Gizon, L. 2013, *ApJ*, 771, 32
- Woodard, M. F. 2007, *ApJ*, 668, 1189
- Zhao, J. 2004, PhD thesis, STANFORD UNIVERSITY
- Zhao, J. & Kosovichev, A. G. 2003, in *ESA Special Publication*, Vol. 517, *GONG+ 2002. Local and Global Helioseismology: the Present and Future*, ed. H. Sawaya-Lacoste, 417–420

## Appendix A: Travel-time measurements

We measure travel-time shifts by minimizing the squared difference between wave displacements in the true and starting supergranule simulations. Given wave displacements  $\xi^{\text{true}}$  and  $\xi^{\text{iter}}$  recorded at a receiver at  $x_r$  and filtered to obtain the wavepacket corresponding to a specific radial order, we define a misfit

$$\eta(x_r, \tau) = \int dt w(x_r, t) \times (\xi^{\text{iter}}(x_r, t) - \xi^{\text{true}}(x_r, t - \tau))^2 \quad (\text{A.1})$$

where  $w(x_r, t)$  is a window function that encloses the wavepackets and isolates them from artifacts that might arise from spatio-temporal periodicity assumed in the simulation. Specifically, we choose the functional form of  $w(x_r, t)$  to be a box function, that is one over the range of the wavepacket and zero outside. We plot one example of a measured wavepacket and window function in Figure A.1 (left panel). The travel-time shift is defined as the value of  $\tau$  that minimizes  $\eta(x_r, \tau)$  (Gizon & Birch, 2002, 2004). For band-limited waveforms sampled beyond twice their Nyquist frequency, this can be computed by equating the temporal derivative of  $\eta(x_r, \tau)$  to zero and solving for  $\tau$ . Expanding  $\eta$  in terms of the time-shift  $\tau$ , suppressing the explicit dependence on the coordinates  $x_r$  and  $t$ , representing the order of derivative using superscripts in parentheses and referring to  $\xi^{\text{true}}(x_r, t) - \xi^{\text{iter}}(x_r, t)$  as  $\delta\xi$ , we obtain

$$\begin{aligned} \eta(x_r, \tau) = & \int dt w(x_r, t) (\delta\xi)^2 \\ & - \tau \int dt w(x_r, t) 2\delta\xi \xi^{\text{true}(1)} \\ & + \tau^2 \int dt w(x_r, t) \left( \delta\xi \xi^{\text{true}(2)} + (\xi^{\text{true}(1)})^2 \right) \\ & + \mathcal{O}(\tau^3). \end{aligned} \quad (\text{A.2})$$

Retaining terms till quadratic order and solving  $\partial_\tau \eta(x_r, \tau) = 0$  leads to a travel-time shift given by

$$\begin{aligned} \delta\tau(x_r) = & \frac{\int dt w(x_r, t) \xi^{\text{true}(1)} \delta\xi}{\int dt w(x_r, t) (\delta\xi \xi^{\text{true}(2)} + (\xi^{\text{true}(1)})^2)} \\ \approx & \int dt \left[ \frac{w(x_r, t) \xi^{\text{true}(1)}}{\int dt' w(x_r, t') (\xi^{\text{true}(1)})^2} \right] \delta\xi. \end{aligned} \quad (\text{A.3})$$

Equation (A.3) is in the form of travel-time shift defined by Gizon & Birch (2002), where the shift  $\delta\tau$  is linear in the displacement difference  $\delta\xi$ . The linear dependence of travel-time shifts on  $\delta\xi$  is important for consistent computation of sensitivity kernels in the first Born approximation. At high flow velocities, however, it is possible that this linear relationship fails to remain a good

approximation (Jackiewicz et al., 2007; DeGrave et al., 2014). For seismic waves with frequency  $\omega$ , the deviation from linearity will be noticeable if the measured travel-time shift  $\delta\tau$  satisfies  $|\omega\delta\tau| \ll 1$ . We have carried out validation tests for by artificially time-shifting a simulated wave field by a typical value measured at surface for each supergranule model, and trying to recover the shift from the series expansion of  $\eta(x_r, \tau)$  truncated at various orders in  $\tau$ . We plot the result of one such validation test in Figure A.1 (right panel). We find that travel-times computed using the linear approximation for the various supergranule models are within 5% of the expected value, the accuracy of the estimate improving with an increase in degree of the truncation. Note that this is the error in travel-time measurement at the first iteration in our inversion. Subsequent iterations improve the flow model and lead to a significant decrease in  $\delta\tau$ , consequently the error in measuring travel-time shifts is also reduced. This ensures that the inverted flow is not affected by the error in measured travel time for the starting model. It might be necessary to take this error into consideration for a linear inversion.

## Appendix B: Spline expansion

We expand the supergranule model from Equation (3) in a basis of B-splines following Equation (10) to obtain a set of coefficients that we invert for. The first step to this expansion is to obtain a set of knots that govern the B-splines. The choice of knots might be important for the inversion to succeed, however further study needs to be carried out to establish this. We choose knots by applying the Dierckx algorithm (Dierckx, 1993) to the true supergranule, but alternate choices of knots derived from an independent, vertically stratified parameter such as sound-speed may also be used. The knots and coefficients are computed using the “`scipy.interpolate`” package of the python programming language, that internally calls the Fortran library FITPACK. The module computes the spline fit by evaluating an optimal set of knots and coefficients, ensuring that the squared  $L_2$  norm of the difference between the data being fit and the spline approximant falls below a specified smoothing factor. Reducing the value of this factor improves the fit; this is achieved by updating the set of knots followed by reevaluating the expansion coefficients. We carry out our inversion in a space spanned by the spline coefficients, therefore the specific choice of a approximant is a tradeoff between the quality of fit and the number of parameters used to obtain the fit. This is why we choose smoothing splines over interpolating ones, since the latter involves a similar fit evaluated without any smoothing and produces a set of knots similar in size to the number of grid points, while the former can be tuned to significantly trim down the size of this set. We select the smoothing factor through experimentation to obtain an accurate representation of

the stream function in the B-spline basis while restraining the number of coefficients to around 10. We list the smoothing parameters and knots for each of the supergranule models in Table B.1. We decide upon quadratic splines as a compromise between a cubic-spline fit that is more oscillatory and a linear-spline fit that is not as smooth and results in a larger parameter space.

We plot the functional form of the B-spline functions for model SG2 in Figure B.1 (left panel). We plot the functional form of the supergranule from Equation (10) as well as the spline approximation to it in Figure B.1 (middle panel), and we plot the error in the approximation in the right panel. We find that smoothing splines are a reasonably good representation of this supergranule model beneath the solar surface.

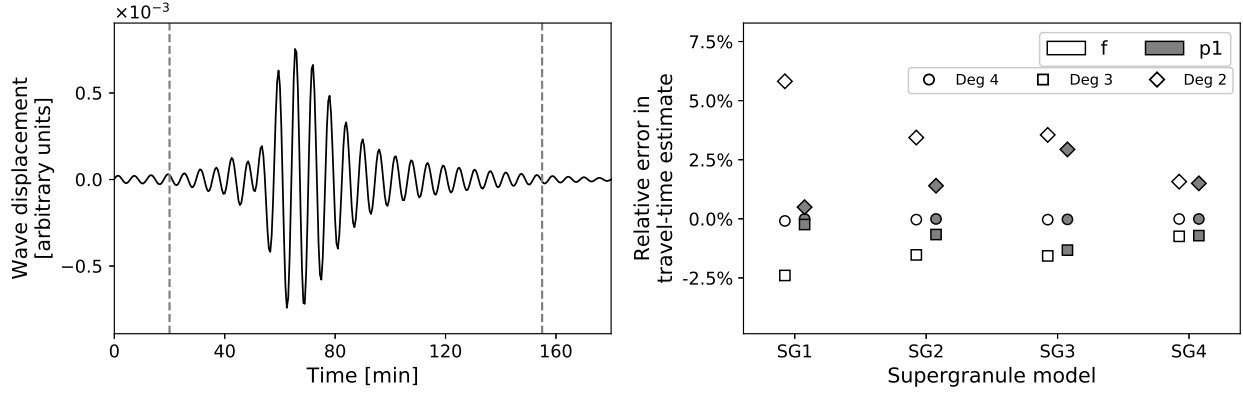


**Figure A.1.** Left: One example of an  $f$ -mode wavepacket measured at a receiver located at  $x_r = 30$  Mm for the supergranule SG1. The extent of the window function  $w(x_r, t)$  is denoted by vertical dashed lines. Right: Relative error in estimated travel-time shifts using wavepackets corresponding to radial orders  $f$  and  $p_1$  (indicated by different colors) as a function of different degree of truncation of Equation (A.2) (indicated by different symbols), for different supergranule models. Truncating Equation (A.2) to quadratic order results in a linear relation between travel-time shift  $\delta\tau$  and wave displacement  $\xi^{\text{iter}}$ , this is plotted with diamonds.

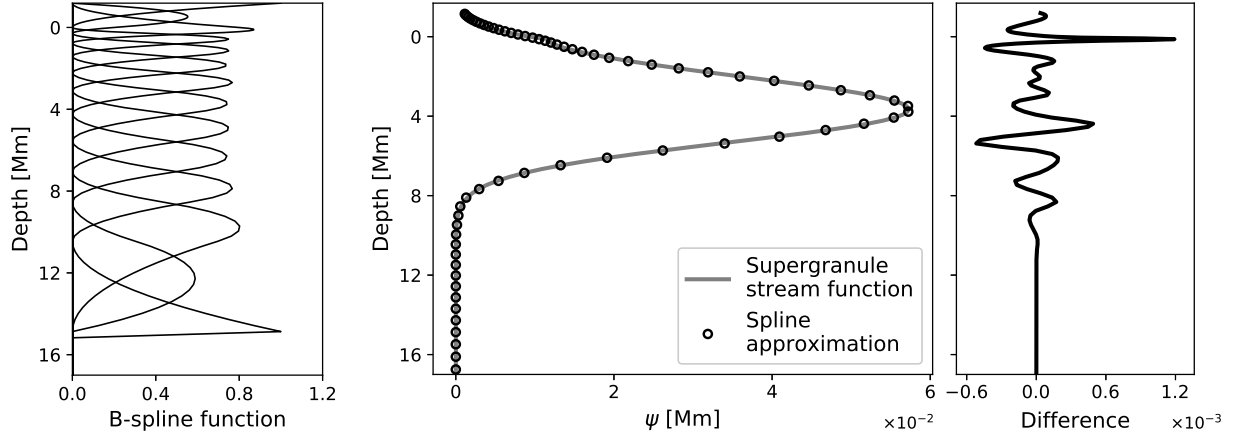


**Figure B.1.** Left: B-spline functions used in the expansion of the supergranule model SG2. Specific choice of knots might be important for the inversion to converge to the correct model. Density of knots with depth is reflective of the degree of stratification. Note that the B-splines are not normalized by the corresponding coefficients. Middle: Supergranule model from Equation (3) (grey solid line) and the smoothing spline approximation to it (black circles). Right: Error in the spline approximation with depth. We see that the smoothing spline approximation is fairly representative of the form of the vertical profile of the supergranule stream function.

**Table B.1.** B-spline parameters used in the inversion

Model	Depth of lower cutoff [Mm]	Smoothing parameter [Mm <sup>2</sup> ]	Number of coefficients	Knots [Mm]
SG1	10	$3.6 \times 10^{-5}$	9	-10.0, -10.0, -10.0, -6.9, -4.5, -3.5, -2.7, -1.3, 0.2, 1.2, 1.2, 1.2
SG2	15	$7.3 \times 10^{-6}$	14	-14.9, -14.9, -14.9, -10.5, -8.5, -7.1, -5.5, -4.2, -3.1, -2.2, -1.4, -0.8, -0.3, -0.0, 1.2, 1.2, 1.2
SG3	15	$2.8 \times 10^{-4}$	13	-14.9, -14.9, -14.9, -12.6, -10.5, -8.5, -7.1, -4.2, -3.1, -2.2, -0.8, -0.3, -0.0, 1.2, 1.2, 1.2
SG4	30	$1.6 \times 10^{-5}$	15	-29.7, -29.7, -29.7, -20.9, -17.4, -14.3, -11.5, -10.2, -9.0, -6.9, -5.0, -2.1, -0.5, -0.0, 0.4, 1.2, 1.2, 1.2